PAPER

Check for updates

Influence of Y-substitution on phase composition and proton uptake of self-generated $Ba(Ce,Fe)O_{3-\delta}$–$Ba(Fe,Ce)O_{3-\delta}$ composites†

Christian Berger, [ID] [ab] Edith Bucher, [ID] [b] Rotraut Merkle, [ID] *[a] Christina Nader, [ID] [b] Judith Lammer, [ID] [c] Werner Grogger,[c] Joachim Maier [ID] [a] and Werner Sitte*[b]

Self-generated composites from the series $BaCe_{1-(x+z)}Fe_xY_zO_{3-\delta}$ with $z = 0.2$ for $0.1 \le x \le 0.6$ and $z = 0$ for Ce : Fe = 1 were obtained by one-pot synthesis. The composites consist of proton and electron conducting phases and are interesting as electrode materials for protonic ceramic fuel and electrolyser cells. X-ray diffraction with quantitative phase analysis and scanning electron microscopy with energy-dispersive X-ray spectroscopy showed that the materials consist of Fe-rich phases and a Ce-rich perovskite phase, which are present in the corresponding proportion depending on the precursor composition (Ce–Fe ratio). Substitution with Y leads to a narrowing of the miscibility gap compared to $BaCe_{1-x}Fe_xO_{3-\delta}$ composites, thus favouring transformation of the composites into single cubic phases at temperatures above 1000 °C. Further, Y influences the mutual solubility of $Fe^{3+/4+}$ and Ce^{4+} in the Ce-rich and Fe-rich phase, respectively, as shown elemental mapping *via* scanning transmission electron microscopy. As only a small proportion of the Y dissolves in the electrolyte-type phase, the increased proton uptake resulting from the incorporation of Y in the Ce-rich phase is limited. Strategies to overcome this limitation by substitution with ions with similar ionic radii, but different basicity, are discussed.

1. Introduction

Solid oxide fuel cells (SOFCs) convert chemical energy contained in various fuels such as hydrogen, methane and other hydrocarbons, into electrical energy. The conversion takes place with high efficiency and without emission of NO_x.[1,2] State-of-the-art SOFCs use oxygen ionic conductors (as electrolytes) and mixed oxygen ionic–electronic conductors (as cathodes).[1–3] In order to obtain sufficiently fast ionic transport, cells based on these materials require relatively high operating temperatures of 700–1000 °C, which causes materials compatibility and degradation issues. With regard to operating temperature and efficiency, protonic ceramic fuel cells (PCFCs) are an interesting alternative to SOFCs.[4–6] PCFCs use proton-conducting oxides, offering the advantages of sufficiently fast ionic transport at relatively low temperatures (300–600 °C) and significantly

ᵃMax Planck Institute for Solid State Research, Heisenbergstraße 1, DE-70569 Stuttgart, Germany. E-mail: r.merkle@fkf.mpg.de; Fax: +49 711 689 1722; Tel: +49 711 689 1768

ᵇChair of Physical Chemistry, Montanuniversitaet Leoben, Franz-Josef-Straße 18, AT-8700 Leoben, Austria. E-mail: werner.sitte@unileoben.ac.at; Fax: +43 3842 402 4802; Tel: +43 3842 402 4800

ᶜInstitute of Electron Microscopy and Nanoanalysis (FELMI), Graz University of Technology & Graz Centre for Electron Microscopy (ZFE), Steyrergasse 17, AT-8010 Graz, Austria

† Electronic supplementary information (ESI) available. See DOI: 10.1039/d1ta07208k

smaller activation energies than oxygen ion conductors.[7] However, as the operating temperature of the cell decreases, the electrochemical performance does as well, due to the reduced catalytic activity of the air electrode. Mixed oxygen ionic–electronic conductors, especially Co-containing perovskites such as $BaCo_{0.7}Fe_{0.22}Y_{0.08}O_{3-\delta}$,[8] $Ba_{0.5}Sr_{0.5}Co_{0.8}Fe_{0.2}O_{3-\delta}$[9] and $La_{0.6}Sr_{0.4}Co_{0.2}Fe_{0.8}O_{3-\delta}$,[10] have been investigated as possible air electrodes in order to improve the catalytic activity at lower temperatures. However, these materials suffer from a comparably low proton uptake. An important goal therefore is to improve the proton uptake and conductivity of potential PCFC cathode materials such that the active zone for oxygen reduction is expanded beyond the gas/electrolyte/cathode triple phase boundary.[11,12]

Different strategies for further optimisation of PCFC cathodes were investigated *e.g.* by using composites of proton-conducting and hole-conducting materials.[13,14] With regard to fabrication of composite cathodes, some disadvantages are associated with conventional mixing of the two phases, such as retention of inhomogeneities and small active areas between the phases (large grain sizes).[15,16] Alternatively, using one-pot self-assembly methods allows one to obtain two homogeneously distributed nanocrystalline phases with complementary functionalities during calcination.[17–23] Cheng *et al.* used Fe substituted $BaCeO_3$ as a model substance for their proof-of-concept study because of its good proton uptake capacity.[24] $BaCe_{0.5}Fe_{0.5}O_{3-\delta}$, which was used as a precursor, decomposes into a Ce-rich

2474 | *J. Mater. Chem. A*, 2022, **10**, 2474–2482

This journal is © The Royal Society of Chemistry 2022

($BaCe_{0.85}Fe_{0.15}O_{3-\delta}$) and a Fe-rich ($BaCe_{0.15}Fe_{0.85}O_{3-\delta}$) thermo-dynamically stable phase. A membrane fabricated from the dual-phase composite thus obtained showed hydrogen permeation flux superior to a membrane obtained by conventional mixing and procession of the two single-phase compounds.[24]

In the present study substitution of $BaCe_{0.5}Fe_{0.5}O_{3-\delta}$ with Y is investigated with the aim of increasing the oxygen vacancy concentration and the basicity of the materials, thereby enhancing the proton uptake capacity. Self-generated nanocomposites obtained from $BaCe_{0.5}Fe_{0.5}O_{3-\delta}$ and $BaCe_{1-(x+0.2)}Fe_xY_{0.2}O_{3-\delta}$ ($0.1 \leq x \leq 0.6$) precursors are characterised with respect to fundamental material properties in order to gain further insights into phase composition and -distribution, as well as proton uptake capacity. Therefore, the obtained trends in proton uptake are correlated with ionic radii and basicity of various B-site substituents (Y, Yb, Sm, Gd) to suggest promising compositions for further studies.

2. Results and discussion

2.1 Phase analysis, lattice parameters and phase formation

X-ray powder diffraction (XRD) patterns of the composites obtained from the precursors $BaCe_{0.5}Fe_{0.5}O_{3-\delta}$ and $BaCe_{1-(x+0.2)}Fe_xY_{0.2}O_{3-\delta}$ ($0.1 \leq x \leq 0.6$) calcined at 1000 °C are shown in Fig. 1a. All these samples exhibit reflections of two different perovskite phases. A quantitative analysis of the relative amounts of the two phases was performed for all investigated composites (Table S1 in the ESI†). While one of these phase is always cubic ($Pm\bar{3}m$ (SG#221), see magnified (011) peak in Fig. 1b), the other perovskite phase belongs to the orthorhombic $GdFeO_3$ structure ($Pmcn$ (SG#62), magnified (002) peak in Fig. 1b) for the Y-free material. For Y-containing samples it acquires a trigonal structure ($R\bar{3}c$ (SG#167), magnified (110) peak in Fig. 1b).

In addition to the change in the space group, the positions of the reflections attributed to the cubic phase, shift towards smaller diffraction angles with decreasing Fe content (Fig. 1b). The positions of the reflections ascribed to the orthorhombic/

trigonal phases are almost independent of the Ce–Fe ratio. Similar trends are observed as a function of the lattice parameters on the Fe content (Fig. 2a). According to energy-dispersive X-ray spectroscopy (EDXS) (see Chapter 2.2), the cubic phase is rich in Fe and the orthorhombic/trigonal phase is rich in Ce. Following Vegard's law,[25] the lattice parameters of the cubic Fe-rich phases (Table S2†) decrease linearly with increasing Fe content of the precursor (Fig. 2a, including also $BaFeO_3$ [26] and $BaFe_{0.8}Y_{0.2}O_3$).[27] For easy comparison, for the Ce-rich phases the pseudo-cubic lattice parameters were calculated (Tables S3 and S4†). Unlike the lattice parameters of the Fe-rich phases, the lattice parameters of the Ce-rich phases show no significant dependence on the Ce content of the precursor, and closely match $BaCeO_3$ and $BaCe_{0.8}Y_{0.2}O_3$ [28] literature data.

The significant differences between the radii of the B-site ions of the ABO_3 perovskite – Ce and Fe – may be considered the main driving force for the separation of the precursor into the cubic and the orthorhombic/trigonal phases. The ionic radii (Ce^{3+} = 1.15 Å, Ce^{4+} = 1.01 Å, Fe^{3+} = 0.785 Å, Fe^{4+} = 0.725 Å and Y^{3+} = 0.9 Å) were taken from Shannon's table of ionic radii[29] under consideration of valence and coordination number (VI for all above mentioned ions).

With the help of spark plasma sintering (SPS), the precursor powders can be compacted to dense ceramic pellets at comparably low temperature. This allows us to follow the lattice parameters and phase distribution as a function of sintering temperature (Fig. S1†). Two-phase composites are obtained at lower temperatures, while for all Y-containing samples single-phase compounds are formed at elevated temperatures. The upper critical mixing temperature depends on the Ce–Fe ratio in the precursor. From these data a tentative phase diagram showing the miscibility gap of $BaCe_{1-(x+0.2)}Fe_xY_{0.2}O_{3-\delta}$ was obtained (Fig. 2b). Cheng et al. studied the Y-free precursor $BaCe_{0.5}Fe_{0.5}O_{3-\delta}$ [24] which forms single phases with Fe-rich (below Ce-concentrations of 15%, $BaCe_{0.15}Fe_{0.85}O_{3-\delta}$) and Ce-rich compositions (below Fe concentrations of 15%, $BaCe_{0.85}Fe_{0.15}O_{3-\delta}$). The Y-free composites remain as two separate phases until the maximum sintering temperature of 1400 °C
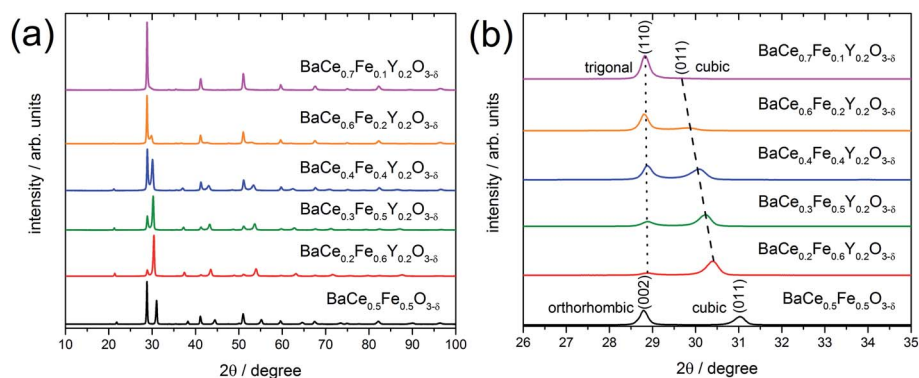

Fig. 1 (a) XRD patterns of composites obtained from calcined precursors of $BaCe_{0.5}Fe_{0.5}O_{3-\delta}$ and $BaCe_{1-(x+0.2)}Fe_xY_{0.2}O_{3-\delta}$ ($0.1 \leq x \leq 0.6$), respectively. (b) The detailed image from the XRD plots on the left (for a selected diffraction angle range) shows an almost constant (002) reflection in the orthorhombic $BaCe_{0.5}Fe_{0.5}O_{3-\delta}$ composite and (110) in the trigonal Y-substituted composites. The contribution of the cubic phase, (011) reflection in both cases, approaches the reflections of the Ce-rich phase with reduced Fe content.
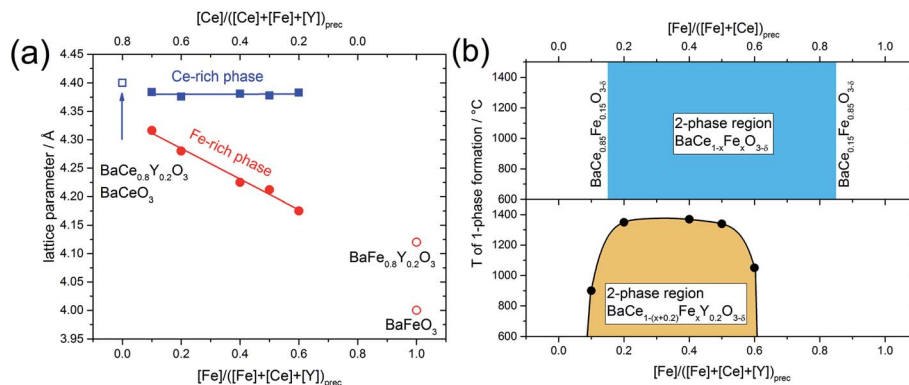
This journal is © The Royal Society of Chemistry 2022

J. Mater. Chem. A, 2022, **10**, 2474–2482 | **2475**

Fig. 2 (a) Lattice parameters of the cubic Fe-rich phase and pseudo-cubic lattice parameter of the trigonal Ce-rich phase as functions of the Fe and Ce content in the annealed precursor powder. The open symbols correspond to lattice parameters of $BaCeO_3$ and $BaCe_{0.8}Y_{0.2}O_3$,[28] $BaFeO_3$ [26] and $BaFe_{0.8}Y_{0.2}O_3$.[27] (b) The phase diagram shows the miscibility gaps of the Y-containing samples and the Y-free samples, respectively. The mutual solubility of Ce in $BaFeO_3$ and *vice versa* was determined to be 15% ($BaCe_{0.15}Fe_{0.85}O_{3-\delta}$ and $BaCe_{0.85}Fe_{0.15}O_{3-\delta}$).[24]

is reached (Fig. 2b and S1;† 1450 °C leads to partial melting). Therefore, it can be concluded that Y-substitution significantly decreases the upper critical mixing temperature in the $Ba(Ce,Fe)O_{3-\delta}$ system. In the case of the Y-substituted compounds, the miscibility gap extends further to the Ce-rich (Fe-poor) side of the phase diagram than in the case of the Y-free compounds. A composite is formed from the precursor $BaCe_{0.7}Fe_{0.1}Y_{0.2}O_{3-\delta}$ (10% Fe on the B-site) at $T < 900\ °C$, whereas the corresponding Y-free compounds with Fe concentrations below of 15% are single-phase. The addition of Y also affects the maximum applicable sintering temperature for the composites. Two-phase composites from $BaCe_{1-(x+0.2)}Fe_xY_{0.2}O_{3-\delta}$ precursors within the limits $0.2 \leq x \leq 0.5$ may be obtained up to relatively high temperatures of $T \leq 1350\ °C$, Fig. 2b. For precursor compositions with either relatively low Fe content ($BaCe_{0.7}Fe_{0.1}$-$Y_{0.2}O_{3-\delta}$) or relatively high Fe content ($BaCe_{0.2}Fe_{0.6}Y_{0.2}O_{3-\delta}$), two-phase composites will only be obtained up to significantly lower sintering temperatures of $T \leq 900\ °C$ and $T \leq 1050\ °C$, respectively, Fig. 2b. Comparing the lattice parameters of the Fe-rich phases of composite powders (using the actual local Fe concentration from Table 1) with those of the single-phase sintered SPS pellets, a linear trend depending on Fe concentration was evident (Fig. S2†).

2.2 Microstructure and elemental distribution

Scanning electron microscopy (SEM)-EDXS were carried out on freshly polished samples to obtain the cation stoichiometry of the precursor phases (Table S5†). Additionally, the average grain sizes of the two-phase composites $BaCe_{0.2}Fe_{0.6}Y_{0.2}O_{3-\delta}$, $BaCe_{0.4}Fe_{0.4}Y_{0.2}O_{3-\delta}$ and $BaCe_{0.6}Fe_{0.2}Y_{0.2}O_{3-\delta}$ precursors were estimated. For this purpose, a sintered pellet was broken and the fracture surface was analysed by using SEM with an in-lens secondary electron detector.

The grain size distribution of self-generated composites was determined by using the image analysis software ImageJ.[30] The exact determination of grain sizes over a representative sample range is difficult because the samples with low Ce content show a certain porosity ($BaCe_{0.2}Fe_{0.6}Y_{0.2}O_{3-\delta}$ and $BaCe_{0.4}Fe_{0.4}Y_{0.2}O_{3-\delta}$) and small precipitates on the grains ($BaCe_{0.2}Fe_{0.6}Y_{0.2}O_{3-\delta}$) (Fig. 3). The morphology of the sample with the highest Ce content differs most clearly due to the increased sintering temperature (1200 °C) compared to the Fe-rich samples (approx. 1000 °C). If one also includes the information from high-angle annular dark-field (HAADF) STEM images (Fig. 4) for $BaCe_{0.2}Fe_{0.6}Y_{0.2}O_{3-\delta}$, a strong variation in grain size especially for the Ce rich phase (bright spots in the HAADF image) is recognized. In addition to the surface morphology images, EDXS maps of the B-site cations were recorded. These show an apparently homogeneous distribution of the cations along the image section of Fig. S3† due to the limitation in the resolution of the SEM-EDXS measurements. No individual grains could be analysed, instead a superposition of the measurement information of several grains was obtained, which is caused by the large inter-action volume generated by the electron beam in SEM-EDXS.

Table 1 B-site composition of the Ce- and Fe-rich phases of $BaCe_{1-(x+z)}Fe_xY_zO_{3-\delta}$ composites obtained from STEM-EDXS point spectra and area scans (see also Fig. S4–S6)

Precursor	Ce-rich phase	Fe-rich phase
$BaCe_{0.5}Fe_{0.5}O_{3-\delta}$ [a]	$Fe_{0.15}Ce_{0.85}$	$Fe_{0.85}Ce_{0.15}$
$BaCe_{0.2}Fe_{0.6}Y_{0.2}O_{3-\delta}$	$Fe_{0.08\pm0.01}Ce_{0.85\pm0.02}Y_{0.07\pm0.01}$	$Fe_{0.64\pm0.03}Ce_{0.15\pm0.02}Y_{0.22\pm0.01}$
$BaCe_{0.4}Fe_{0.4}Y_{0.2}O_{3-\delta}$	$Fe_{0.10\pm0.01}Ce_{0.82\pm0.03}Y_{0.09\pm0.02}$	$Fe_{0.53\pm0.01}Ce_{0.22\pm0.01}Y_{0.25\pm0.02}$
$BaCe_{0.6}Fe_{0.2}Y_{0.2}O_{3-\delta}$	$Fe_{0.12\pm0.02}Ce_{0.72\pm0.03}Y_{0.16\pm0.01}$	$Fe_{0.39\pm0.03}Ce_{0.32\pm0.04}Y_{0.29\pm0.01}$

[a] Data for $BaCe_{0.5}Fe_{0.5}O_{3-\delta}$ was taken from Cheng *et al.*[24]

2476 | *J. Mater. Chem. A*, 2022, **10**, 2474–2482

This journal is © The Royal Society of Chemistry 2022
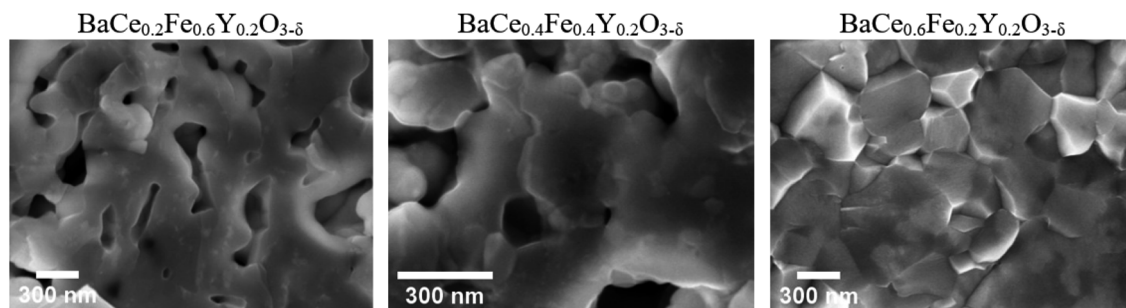
Fig. 3 SEM images of $BaCe_{0.2}Fe_{0.6}Y_{0.2}O_{3-\delta}$, $BaCe_{0.4}Fe_{0.4}Y_{0.2}O_{3-\delta}$ and $BaCe_{0.6}Fe_{0.2}Y_{0.2}O_{3-\delta}$ composite ceramics (SPS sintering, Table S6†) recorded along fracture planes with an in-lens secondary electron detector.

Scanning transmission electron microscopy (STEM)-EDXS was carried out to determine the cation stoichiometry and distribution within the individual phases in the composites with high lateral resolution. Fig. 4 shows STEM-images images (using a HAADF detector) of two-phase composites obtained from $BaCe_{0.2}Fe_{0.6}Y_{0.2}O_{3-\delta}$, $BaCe_{0.4}Fe_{0.4}Y_{0.2}O_{3-\delta}$ and $BaCe_{0.6}Fe_{0.2}Y_{0.2}O_{3-\delta}$ precursors and the respective cation distributions. The grain sizes of the individual phases are in the sub-micrometer range. The reduced grain growth, compared to the Y-free composite,[24] is probably mainly due to the use of SPS as a sintering method (fast densification in short time at moderate temperature). In the composite formed from the $BaCe_{0.6}Fe_{0.2}Y_{0.2}O_{3-\delta}$ precursor, small amounts of the impurity phase Y_2O_3 are observed (bright spots in the Y-map). However, since the Y_2O_3 impurity phase was not detected in the XRD measurements, the fraction of this phase is rather small and therefore not significant for the investigated material properties.
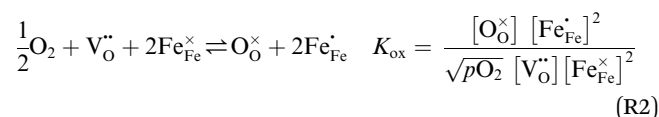
The mutual solubility of $Fe^{3+/4+}$ and Ce^{4+} ions, as well as the distribution of Y in the two phases, was investigated by STEM-EDXS (Table 1). More than 70 single spectra and 10 area scans each were measured within grains of the different phases of the composites in order to describe the cation composition statistically well (Fig. S4–S6†). Data from STEM-EDXS indicate that Y incorporation is more favourable in the Fe-rich phase than in the Ce-rich phase (as seen in Fig. S7†). The addition of Y leads to a decreased Fe and increased Ce content in the Fe-rich phase (see Fig. S8a†) compared to the Fe-rich phase of the Y-free composite. Regarding the Ce-rich phase, the Ce and Fe contents of the composites containing Y are similar (see Fig. S8b†) to those of the Y-free composite. The Ce-rich phase in the $BaCe_{1-x}Fe_xY_{0.2}O_{3-\delta}$ composites remains within the single-phase region indicated in Fig. 2b. However, for the Fe-rich phase higher Ce contents are found compared to Fig. 2b. This is probably related to the increased Y concentrations, which expand the lattice of the ferrate perovskite and thus facilitate Ce incorporation. The composition of the Fe-rich phase depends on the overall cation composition (*cf.* also variation of the lattice parameters in Fig. 2a), in particular for $BaCe_{0.6}Fe_{0.2}Y_{0.2}O_{3-\delta}$ rather high Y and Ce contents appear in the Fe-rich phase. In Chapter 2.3, the reasons for the element distribution between the perovskite phases are discussed.
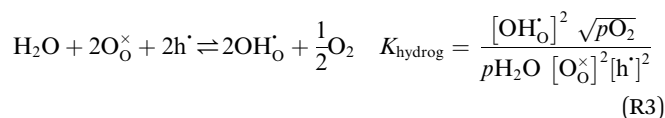
2.3 Trends in water uptake

The water uptake of perovskites is primarily represented by the acid–base reaction (R1) (hydration reaction).[27]

$$H_2O + V_O^{\bullet\bullet} + O_O^x \rightleftharpoons 2\,OH_O^{\bullet} \qquad K_{hydrat} = \frac{[OH_O^{\bullet}]^2}{pH_2O\,[V_O^{\bullet\bullet}]\,(3 - [V_O^{\bullet\bullet}])} \tag{R1}$$
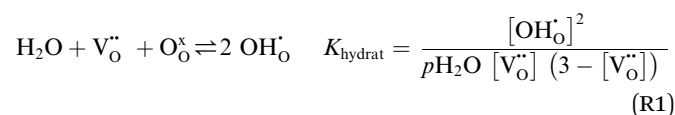
Two protonic defects $OH_O^{\bullet}$ are formed by dissociative incorporation of water into an oxygen vacancy $V_O^{\bullet\bullet}$. With perovskites containing redox active transition metal ions (with mixed valence, *e.g.* $Fe^{3+/4+}$) at the B-site, the oxygen exchange reaction (redox reaction) must also be considered ((R2)).

$$\frac{1}{2}O_2 + V_O^{\bullet\bullet} + 2Fe_{Fe}^x \rightleftharpoons O_O^x + 2Fe_{Fe}^{\bullet} \qquad K_{ox} = \frac{[O_O^x]\,[Fe_{Fe}^{\bullet}]^2}{\sqrt{pO_2}\,[V_O^{\bullet\bullet}][Fe_{Fe}^x]^2} \tag{R2}$$

In Fe-rich perovskites, the dominant electronic charge carriers under oxidising conditions (high pO_2) are p-type defects (electron holes; $h^{\bullet}$), which are transferred between the iron ions Fe_{Fe}^x (Fe^{3+}) and $Fe_{Fe}^{\bullet}$ (Fe^{4+}). The combination of oxygenation and hydration reaction ((R1) and (R2)) yields proton uptake by a redox reaction ("hydrogenation"):[31–33]

$$H_2O + 2O_O^x + 2h^{\bullet} \rightleftharpoons 2OH_O^{\bullet} + \frac{1}{2}O_2 \qquad K_{hydrog} = \frac{[OH_O^{\bullet}]^2\,\sqrt{pO_2}}{pH_2O\,[O_O^x]^2[h^{\bullet}]^2} \tag{R3}$$

From (R3) it is evident that high concentrations of protonic defects ($OH_O^{\bullet}$) and high electron hole concentrations show opposite tendencies. High concentrations of both $OH_O^{\bullet}$ and $h^{\bullet}$ in a single-phase material are therefore difficult to achieve. Depending on the experimental conditions, either reaction (R1) or (R2) may predominate. The hydration reaction is preferred when the sample fulfils the criterion $2\,[V_O^{\bullet\bullet}] > [Fe_{Fe}^{\bullet}]$. To measure the proton uptake exclusively in the regime of predominant hydration, the samples need to be quenched to suppress the redox reaction (see Experimental chapter 3.3).[27] The proton concentration was obtained from the change in
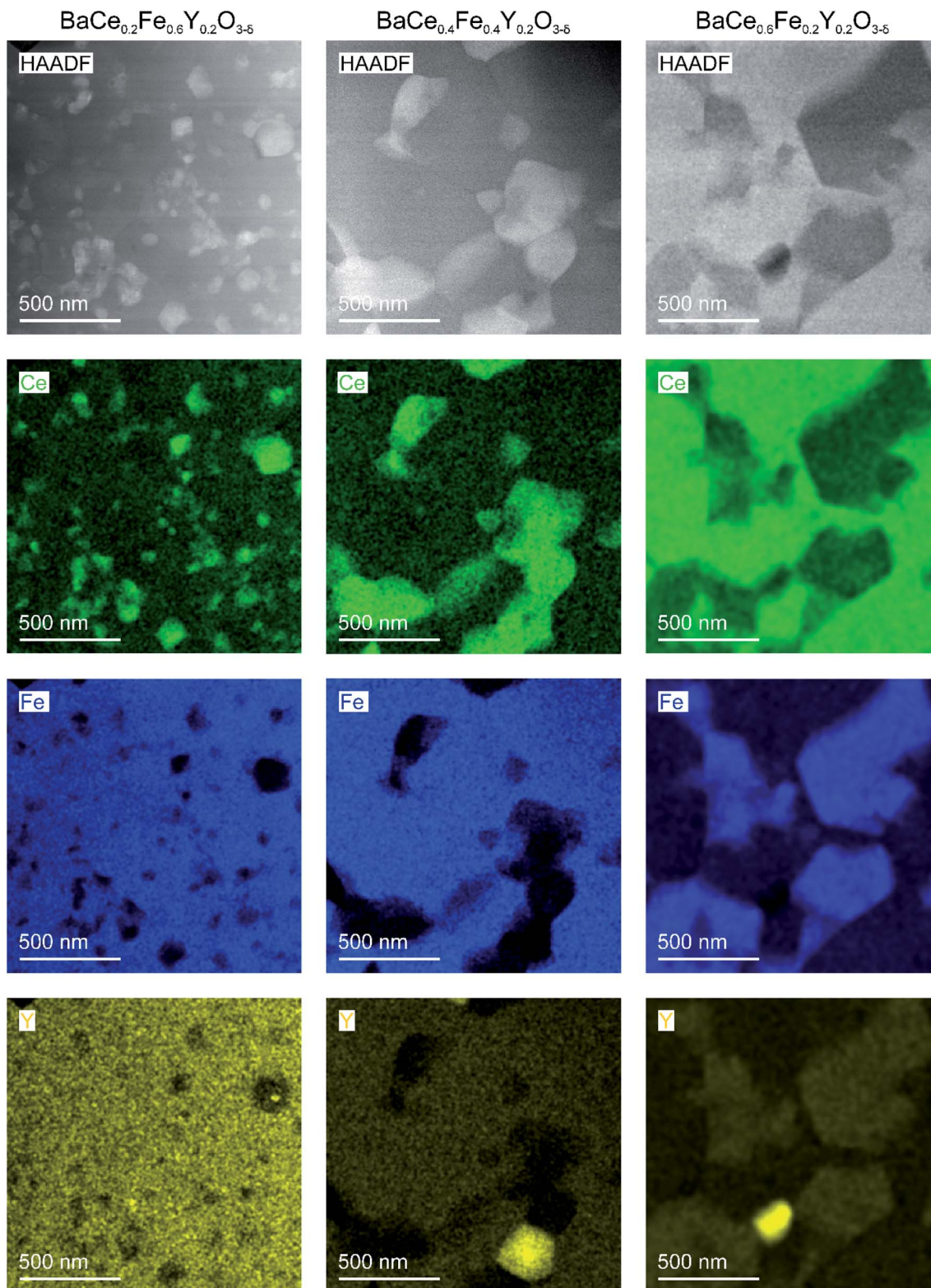
Fig. 4 STEM-HAADF images with EDXS elemental maps for selected cations of composite ceramics obtained from precursors of $BaCe_{0.2}Fe_{0.6}Y_{0.2}O_{3-\delta}$ (left column), $BaCe_{0.4}Fe_{0.4}Y_{0.2}O_{3-\delta}$ (in the middle) and $BaCe_{0.6}Fe_{0.2}Y_{0.2}O_{3-\delta}$ (right column) by spark plasma sintering (conditions given in Table S6†). The bright grains in the Y maps are occasional Y-rich precipitates.

sample mass after pH_2O steps at constant T, under the assumption that (R1) predominates (which is ensured by the experimental conditions used). However, the distribution of the water uptake between the two phases in the composite is not easily accessible (thus no ΔH^0_{hydrat}, ΔS^0_{hydrat} can be extracted).

2478 | *J. Mater. Chem. A*, 2022, **10**, 2474–2482
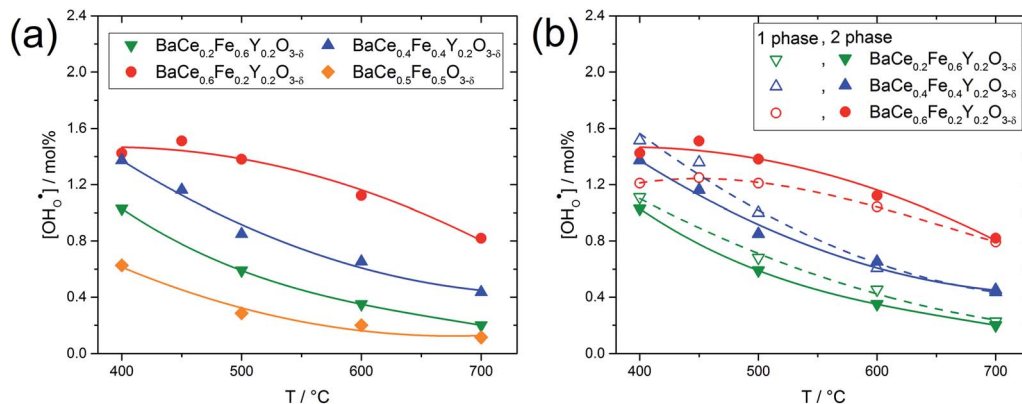
This journal is © The Royal Society of Chemistry 2022

Fig. 5 (a) Proton concentrations of two-phase composites with frozen-in oxygen stoichiometry in 17 mbar pH$_2$O (samples were quenched from 700 °C in N$_2$) as a function of temperature. (b) Comparison of the proton concentration of two-phase composites (samples sintered at temperatures below the upper critical mixing temperature; closed symbols and full lines) and the corresponding single phases (samples sintered at temperatures above the upper critical mixing temperature; open symbols and dashed line). The lines are guidelines to the eye.

Fig. 5a shows the proton concentration of selected composites. As the temperature decreases from 700 °C to 400 °C, the proton concentration within a composite increases moderately. Two important trends can be noted: (i) the addition of Y increases the proton uptake of all composites investigated, and (ii) with increased Ce content in the composite, proton uptake increases. The reason for the decreasing slope of the proton uptake curve for BaCe$_{0.6}$Fe$_{0.2}$Y$_{0.2}$O$_{3-\delta}$ from 450 °C to 400 °C is not clear yet.

Fig. 5b compares the proton uptake for selected Ce–Fe ratios of the two-phase composites (closed symbols) and the corresponding single phases (obtained by sintering the composites at elevated temperatures where complete miscibility occurs). The temperatures for achieving single-phase samples can be recognized in Fig. S1.† For a given Ce–Fe ratio, the proton concentration of the two-phase composite and the single-phase material is relatively similar. This could be due to the preferential solubility of Y in the Fe-rich phases of the composites and the correspondingly lower Y concentrations in the Ce-rich phases (see Table 1). Lower Y concentrations in the Ce-rich phases reduce the concentration of oxygen vacancies as well as the basicity,[27] both effects being negative for proton uptake. It has already been shown experimentally that the water uptake of electrolytes[7] and mixed-conducting perovskites[27] depends on the basicity of the respective materials. Recent DFT calculations support this statement and show that the proton affinity varies more strongly with material composition than with hydroxide affinity. Thus, the proton affinity dominates the trend of hydration enthalpy, and the proton affinity correlates with the basicity of the material.[34]

Fig. 6 shows the proton concentration as a function of Fe content at 500 °C. The increase in proton uptake is evident in comparison of the Y-containing composites (closed symbols) with the Y-free composite (open symbol). The proton concentration decreases significantly with increasing Fe content in the precursor, reaching a plateau for $x \geq 0.4$ in BaCe$_{1-(x+0.2)}$Fe$_x$Y$_{0.2}$O$_{3-\delta}$. A possible explanation for this trend might be a reduced basicity of the material (Fe^{3+} is more acidic than Ce^{4+}, see also Fig. 7). The decrease in the relative amount of the Ce-rich phase (i.e. the dominant proton-conducting phase in the composites) with

increasing Fe content in the precursor could also contribute to the decrease in [OH$_O^\bullet$]. Both effects would restrict the proton conduction in Ce-rich percolating paths in the composite. When redox active transition metals are added to the B-site of the perovskite, the proton uptake decreases. This was demonstrated e.g. for (La,Sr)(Sc,Fe)O$_3$,[35] and has also been shown for Ba(Zr$_{0.88-x}$Fe$_x$Y$_{0.12}$)O$_3$.[12] This effect is attributed to the higher covalence of Fe–O bonds (electron density is drawn from oxygen to iron and thus the basicity of the oxygen is reduced).[36]

In comparison with single-phase proton-conducting ferrates/cobaltates (Ba$_{0.85}$La$_{0.15}$FeO$_{3-\delta}$ [OH$_O^\bullet$] = 0.1 mol%, Ba$_{0.50}$Sr$_{0.5}$FeO$_{3-\delta}$ [OH$_O^\bullet$] = 0.2 mol% and Ba$_{0.5}$Sr$_{0.5}$Co$_{0.8}$Fe$_{0.2}$O$_{3-\delta}$ [OH$_O^\bullet$] = 0.1 mol%;[37] all at T = 500 °C and pH$_2$O = 17 mbar), the proton uptake of the self-generated BaCe$_{1-(x+0.2)}$Fe$_x$Y$_{0.2}$O$_{3-\delta}$ composites is considerably higher (0.6–1.4 mol% at T = 500 °C and pH$_2$O = 17 mbar). A better understanding of the cation distribution within the two phases of the self-generated composites could lead to a further optimization of the proton uptake by tailored compositional variations.

Substitution with Y^{3+} increases the oxygen vacancy concentration and the basicity in both Ce- and Fe-rich phases. If Y is
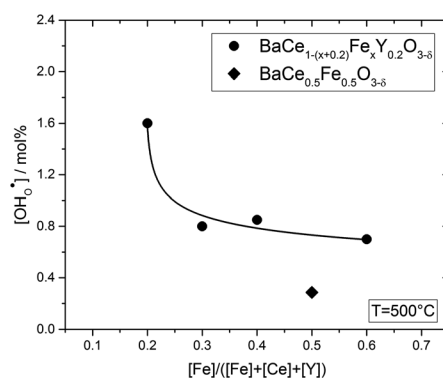
Fig. 6 Proton concentration of composites obtained from precursors of BaCe$_{0.5}$Fe$_{0.5}$O$_{3-\delta}$ (open symbol) and BaCe$_{1-(x+0.2)}$Fe$_x$Y$_{0.2}$O$_{3-\delta}$ (0.2 $\leq x \leq$ 0.6) (closed symbols) as a function of Fe content for T = 500 °C. The line connecting the circles is a guide to the eye.

This journal is © The Royal Society of Chemistry 2022

J. Mater. Chem. A, 2022, **10**, 2474–2482 | **2479**

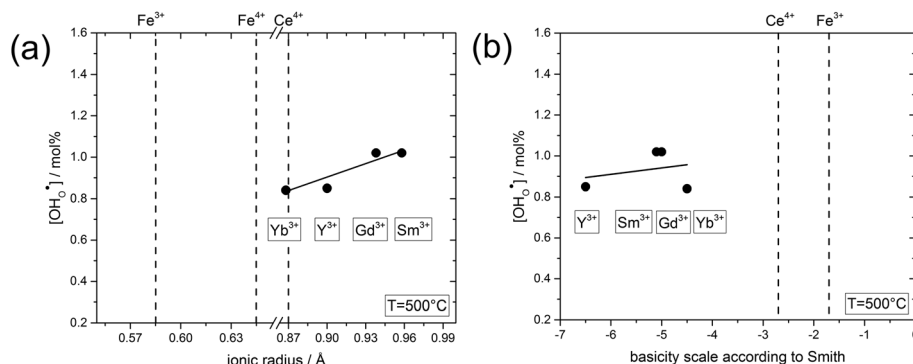**Fig. 7** (a) Proton concentration at 500 °C of composites obtained from precursors of $BaCe_{0.4}Fe_{0.4}B_{0.2}O_{3-\delta}$ (B = Yb, Y, Gd or Sm) as a function of the ionic radius[29] of B. (b) Proton concentration at 500 °C of composites obtained from precursors of $BaCe_{0.4}Fe_{0.4}B_{0.2}O_{3-\delta}$ (B = Yb, Y, Gd or Sm) as a function of the basicity[39] of the binary oxides of B.

dissolved preferentially in the Fe-rich phase, only a small fraction of the Y will occur in the Ce-rich phase (which is the phase with the higher degree of hydration) and thus the proton uptake of the composite is only slightly improved (see Fig. 5 and 6). It is known from single-phase perovskite materials such as $BaFe_{0.8}Y_{0.2}O_{3-\delta}$ and $Ba_{0.95}La_{0.05}Fe_{0.8}Zn_{0.2}O_{3-\delta}$[27] that partial substitution of Fe by oversized, redox-inactive cations such as Y^{3+}, Zn^{2+} significantly increases the proton uptake of these phases. However, in absolute numbers the increase in proton uptake by Y substitution in the Fe-rich phase is only moderate, and cannot overcompensate the decrease of proton uptake by decreased Y levels in the Ce-rich phase of the present composites (the detailed variation of proton uptake in single-phase perovskite materials with Ce, Fe and Y concentrations will be published separately). Thus, in the present $BaCe_{1-(x+0.2)}Fe_xY_{0.2}O_{3-\delta}$ composites the proton uptake is less than estimated from a mixture of $BaCe_{0.8}Y_{0.2}O_{2.9}$ and $BaFe_{0.8}Y_{0.2}O_{3-\delta}$. On the other hand, the partial dissolution of Fe in the cerate and Ce in the ferrate phase tunes both phases towards becoming triple conductors and thus has the potential to widen the active region for oxygen reduction in a composite PCFC cathode beyond the actual three phase boundary.

In the following, the influence of the ionic radius and the basicity on the proton uptake is discussed for Y and other substituents in $BaCe_{0.4}Fe_{0.4}B_{0.2}O_{3-\delta}$ composites (B = Y, Yb, Sm, Gd) (Fig. 7). The key for the proton uptake is the distribution of the acceptor between the Ce-rich and the Fe-rich phase. The mismatch in the ionic radii of Y^{3+} (0.9 Å) and Ce^{4+} (0.87 Å) can lead to strain in the Ce-rich phase, although the size effect is more severe for Y in the Fe-rich phase. Intermixing of the cations, including dissolution of part of the Y^{3+} in the Fe-rich phase, may be a means to reduce this strain,[38] but leads to a decrease in the proton uptake. Ytterbium was explored as an alternative substituent ion for the $Ba(Ce,Fe)O_{3-\delta}$ series to counteract strain-induced cation intermixing, since Yb^{3+} (0.868 Å) has almost the same ionic radius as Ce^{4+}. However, this approach did not result in any significant increase in proton uptake, see Fig. 7a. Subsequently, two substituents with relatively large ionic radii, Gd^{3+} (0.94 Å) and Sm^{3+} (0.96 Å) were tried, but again no significant change in proton uptake was

observed. Thus, it appears that the ionic radius of the substituent ion plays a subordinate role for the distribution of the acceptor, and therefore for the proton uptake of the composite. Another driving force for the formation of the self-generated composites is the balance in basicity of the two phases due to the solubility of Ce in the Fe-rich phase and *vice versa* and the Y distribution.[39] The acceptor distribution is governed by an acid–base reaction, whereby the larger (more basic) ion experience a stronger driving force for the incorporation into the Fe-rich phase. As evident from Fig. 7b, the substituent ions studied have a relatively high basicity compared to the less basic Fe. Thus, it may be favourable for Y, Yb, Sm, Gd to dissolve in the Fe-rich phase in the sense of an acid–base reaction. Consequently, a more acidic three-valent ion, which should also have a similar ionic radius to Ce^{4+}, may have a higher affinity to dissolving in the Ce-rich phase of $Ba(Ce,Fe)O_{3-\delta}$ based composites, and thus improve the proton uptake. Systematic studies of the structure–property relations of composites substituted in this way will be the subject of future work.

3. Experimental

3.1 Synthesis

Nanocomposite powders were obtained for $BaCe_{1-(x+z)}Fe_xY_zO_{3-\delta}$ with $z = 0.2$ for $0.1 \leq x \leq 0.6$ and $z = 0$ for Ce : Fe = 1, using a sol–gel method ("one-pot" synthesis) followed by thermal treatment. Stoichiometric amounts of the corresponding metal-nitrates ($Ba(NO_3)_2$, $Ce(NO_3)_3 \cdot 6H_2O$, $Y(NO_3)_2 \cdot 6H_2O$ and $Fe(NO_3)_3 \cdot 9H_2O$) (all from Sigma Aldrich, analytical grade quality) were mixed with distilled H_2O in a stainless steel vessel. Anhydrous citric acid and EDTA (one mole each per cation) were added after the metal-nitrates were completely dissolved. Then, a 25% aqueous NH_3 solution was added until pH = 8 was reached and a clear dark blue solution was obtained. The temperature was continuously increased to remove water and form a gel. Self-ignition and combustion of the dried gel occurred at approximately 500 °C. The raw ash was crushed in an agate mortar and calcined at 1000 °C for 10 h (5 K min^{-1} ramps for heating and cooling) in air. During this process, the precursor decomposed into a mixture of two crystalline phases,

2480 | *J. Mater. Chem. A*, 2022, **10**, 2474–2482

This journal is © The Royal Society of Chemistry 2022

as confirmed after calcination by XRD. For all further measurements, the powders were dry ground in a zirconia ball mill and sintered in a graphite mold using a SPS uniaxial hot-press (FCT Systems GmbH, Germany). Parameters and densities from the SPS process are shown in ESI Table S6.† Long-term annealing experiments on the sintered pellets were performed to further explore the stability of the self-generated composites (see Fig. S9 in the ESI†).

3.2 Microstructural characterisation

XRD analysis of the calcined powders was performed with a BRUKER-AXS D8 Advance ECO diffractometer using a Cu Kα radiation source ($\lambda = 1.5406$ Å) operated at 40 kV and 25 mA. The diffractogram was recorded at room temperature with a scanning rate of 0.01° s^{-1} with 2 s acquisition time per step. Lattice parameters of the room temperature phases were obtained from fitting the peak positions to either a cubic unit cell (space group $Pm\bar{3}m$) for one phase, and an orthorhombic unit cell (space group $Pmcn$ for the Y-free sample) or a trigonal unit cell (space group $R\bar{3}c$ for the Y-containing samples) for the other phase. Whole diffraction pattern profile fitting using LeBail analysis was performed by using the commercial software TOPAS.[40–42]

Inductively coupled plasma optical emission spectrometry (ICP-OES, SPECTRO CIROS from SPECTRO Analytical Instruments GmbH) was used to determine the average cation composition of BCFY samples. For the analyses specific sample amounts were dissolved in hydrochloric acid. The obtained cation compositions are given in Tables S7 and S8.†

Spatial cation distributions and local cation compositions were determined by EDXS in a scanning electron microscope (Zeiss Merlin) operated at 10 kV equipped with an Oxford Instruments Ultim Extreme detector. For the applied electron energy, penetration depths of 1–5 μm are expected.

Sample preparation for STEM investigations was carried out with a focused ion beam (FIB) microscope FEI NOVA 200 NanoLab. The TEM lamellae were cut out of the polished surfaces of SPS densified pellets. STEM investigations were performed with an FEI TITAN3 G2 60–300 at 300 kV accelerating voltage. The microscope is equipped with a C$_s$-probe corrector and a Super-X detector by FEI. STEM images were recorded with a HAADF detector. The software packages GMS 3 (Gatan) and Velox 2 (Thermo Fisher Scientific) were used to acquire HAADF images and EDXS spectrum images. STEM-EDXS measurements were performed on grains, which were not aligned along major zone axes with respect to the electron beam in order to avoid channelling effects during the measurement.[43]

3.3 Thermogravimetry

Thermogravimetry (STA449C Jupiter, Netzsch, Germany) was carried out with approximately 0.5–1 g of sample (sintered pellet crushed to particles) in an alumina crucible with an N$_2$ flow of 60 ml min^{-1}. In order to implement humid conditions the water partial pressure (pH$_2$O) was adjusted by bubbling the gas through a thermostated water evaporator (the flow of 10 ml min^{-1} "protective gas" through the balance compartment of the STA449 was always kept dry). For isothermal pH$_2$O changes,

the measured buoyancy effects were negligible. In order to "freeze" the oxygen exchange reaction, the particles were quenched from 700 °C in dry N$_2$ so that all Fe is present as Fe^{3+} and then cooled rapidly (20 K min^{-1}) to the desired temperature at which the proton uptake is to be determined. An appropriate particle size is essential for the suppression of the surface controlled reaction of oxygen incorporation. The optimal particle size (here: 100–250 μm) is a compromise between reduced surface reaction (low pO$_2$ and low T) and a reasonable time (10–100 min) for the kinetically more facile water uptake reaction to reach equilibrium (see Fig. S10†). This method avoids complications from hole-proton defect interactions and the long equilibration times at low temperatures as described in Zohourian *et al.*[27]

4. Summary and conclusions

Self-generated BaCe$_{1-(x+z)}$Fe$_x$Y$_z$O$_{3-\delta}$ composites ($z = 0.2$ for $0.1 \leq x \leq 0.6$ and $z = 0$ for Ce : Fe = 1) were synthesized and characterized with respect to their chemical composition, phase stability and water uptake. A miscibility gap with an upper critical mixing temperature of ∼1350 °C leads to the formation of two-phase composites of all investigated precursor compositions containing Y. The composites show variable phase ratios of the cubic Fe-rich and the trigonal Ce-rich phase, with the cubic phase dominating at higher temperatures. By exposure to temperatures above the upper critical mixing temperature, single-phase perovskites are formed, with the cation stoichiometry corresponding to that of the precursor. Scanning transmission electron microscopy and scanning electron microscopy with energy-dispersive X-ray spectroscopy showed some mutual dissolution of Fe and Ce in the respective other phase, and that Y dissolves preferentially in the Fe-rich phase of the composites. The proton concentration in the Ce-rich phase of the composites is significantly lowered by the Fe incorporation. In addition, the lower degree of Y substitution in the Ce-rich phase decreases proton uptake, resulting in similar proton concentrations in single-phase and composite materials with identical overall cation composition. Knowledge of the local cation concentration of the individual phases is particularly important in the present case, since it affects properties like phase formation and water uptake. Finally, reasons for the preferred distribution of Y in the Fe-rich phase were discussed. A possible explanation is the tendency of the coexisting phases to balance their respective basicity.

Author contributions

Christian Berger: conceptualization, methodology, investigation, writing – original draft, writing – review & editing, visualization. Edith Bucher: conceptualization, writing – review & editing, supervision, project administration, funding acquisition. Rotraut Merkle: conceptualization, methodology, investigation, writing – review & editing, supervision. Christina Nader: investigation, writing – review & editing. Judith Lammer: investigation, writing – review & editing, visualization. Werner Grogger: writing – review & editing. Joachim Maier:

This journal is © The Royal Society of Chemistry 2022

J. Mater. Chem. A, 2022, **10**, 2474–2482 | **2481**

conceptualization, writing – review & editing, supervision. Werner Sitte: conceptualization, writing – review & editing, supervision.

Conflicts of interest

The authors declare that they have no known competing financial interests or personal relationships that could have appeared to influence the work reported in this paper.

Acknowledgements

References

1 S. C. Singhal and K. Kendall, *High temperature solid oxide fuel cells: fundamentals, design and applications*, Elsevier Advanced Technology, Oxford, UK, 2004.
2 K.-D. Kreuer, *Fuel cells – Selected entries from the encyclopedia of sustainability science and technology*, Springer-Verlag, New York, 1st edn, 2013.
3 K. Kendall and M. Kendall, *High-temperature Solid Oxide Fuel Cells for the 21st Century*, Academic Press, Oxford, UK, 2016.
4 H. Zhu and R. J. Kee, *J. Electrochem. Soc.*, 2017, **164**, F1400–F1411.
5 Y. Matsuzaki, Y. Tachikawa, T. Somekawa, T. Hatae, H. Matsumoto, S. Taniguchi and K. Sasaki, *Sci. Rep.*, 2015, **5**, 12640.
6 J. H. Shim, *Nat. Energy*, 2018, **3**, 168–169.
7 K. D. Kreuer, *Annu. Rev. Mater. Res.*, 2003, **33**, 333–359.
8 W. He, X. Wu, G. Yang, H. Shi, F. Dong and M. Ni, *ACS Energy Lett.*, 2017, **2**, 301–305.
9 D. Chen and Z. Shao, *Int. J. Hydrogen Energy*, 2011, **36**, 6948–6956.
10 L. Nie, M. Liu, Y. Zhang and M. Liu, *J. Power Sources*, 2010, **195**, 4704–4708.
11 M. Papac, V. Stevanović, A. Zakutayev and R. O'Hayre, *Nat. Mater.*, 2021, **20**, 301–313.
12 R. Merkle, M. F. Hoedl, G. Raimondi, R. Zohourian and J. Maier, *Annu. Rev. Mater. Res.*, 2021, **51**, 461–493.
13 L. Yang, Z. Liu, S. Wang, Y. Choi, C. Zuo and M. Liu, *J. Power Sources*, 2010, **195**, 471–474.
14 E. Fabbri, L. Bi, D. Pergolesi and E. Traversa, *Energy Environ. Sci.*, 2011, **4**, 4984–4993.
15 G. Yang, C. Su, H. Shi, Y. Zhu, Y. Song, W. Zhou and Z. Shao, *Energy Fuels*, 2020, **34**, 15169–15194.
16 J. Druce, H. Téllez, T. Ishihara and J. A. Kilner, *Faraday Discuss.*, 2015, **182**, 271–288.
17 X. Zhu, H. Wang and W. Yang, *J. Membr. Sci.*, 2008, **309**, 120–127.
18 W. Fang, F. Liang, Z. Cao, F. Steinbach and A. Feldhoff, *Angew. Chem., Int. Ed.*, 2015, **54**, 4847–4850.
19 W. Fang, F. Steinbach, Z. Cao, X. Zhu and A. Feldhoff, *Angew. Chem.*, 2016, **128**, 8790–8793.
20 W. Fang, C. Zhang, F. Steinbach and A. Feldhoff, *Angew. Chem., Int. Ed.*, 2017, **56**, 7584–7588.
21 L. Rioja-Monllor, C. Bernuy-Lopez, M.-L. Fontaine, T. Grande and M.-A. Einarsrud, *Materials*, 2019, **12**, 3441.
22 Y. Song, Y. Chen, W. Wang, C. Zhou, Y. Zhong, G. Yang, W. Zhou, M. Liu and Z. Shao, *Joule*, 2019, **3**, 2842–2853.
23 Z. Zhao, J. Cui, M. Zou, S. Mu, H. Huang, Y. Meng, K. He, K. S. Brinkman and J. Tong, *J. Power Sources*, 2020, **450**, 227609.
24 S. Cheng, Y. Wang, L. Zhuang, J. Xue, Y. Wei, A. Feldhoff, J. Caro and H. Wang, *Angew. Chem., Int. Ed.*, 2016, **55**, 10895–10898.
25 L. Vegard, *Z. Phys.*, 1921, **5**, 17–26.
26 M. Erchak, I. Fankuchen and R. Ward, *J. Am. Chem. Soc.*, 1946, **68**, 2085–2093.
27 R. Zohourian, R. Merkle, G. Raimondi and J. Maier, *Adv. Funct. Mater.*, 2018, **28**, 1801241.
28 L. Malavasi, H. Kim and T. Proffen, *J. Appl. Phys.*, 2009, **105**, 123519.
29 R. D. Shannon, *Acta Crystallogr., Sect. A: Cryst. Phys., Diffr., Theor. Gen. Crystallogr.*, 1976, **32**, 751–767.
30 C. A. Schneider, W. S. Rasband and K. W. Eliceiri, *Nat. Methods*, 2012, **9**, 671.
31 D. Poetzsch, R. Merkle and J. Maier, *Adv. Funct. Mater.*, 2015, **25**, 1542–1557.
32 D. Poetzsch, R. Merkle and J. Maier, *Phys. Chem. Chem. Phys.*, 2014, **16**, 16446–16453.
33 D. Poetzsch, R. Merkle and J. Maier, *Faraday Discuss.*, 2015, **182**, 129–143.
34 T. S. Bjørheim, M. F. Hoedl, R. Merkle, E. A. Kotomin and J. Maier, *J. Phys. Chem. C*, 2020, **124**, 1277–1284.
35 D. Han, Y. Okumura, Y. Nose and T. Uda, *Solid State Ionics*, 2010, **181**, 1601–1606.
36 M. F. Hoedl, D. Gryaznov, R. Merkle, E. A. Kotomin and J. Maier, *J. Phys. Chem. C*, 2020, **124**, 11780–11789.
37 R. Zohourian, *PhD thesis*, University of Stuttgart, 2018.
38 F. Baiutti, F. Chiabrera, M. Acosta, D. Diercks, D. Parfitt, J. Santiso, X. Wang, A. Cavallaro, A. Morata, H. Wang, A. Chroneos, J. MacManus-Driscoll and A. Tarancon, *Nat. Commun.*, 2021, **12**, 2660.
39 D. W. Smith, *J. Chem. Educ.*, 1987, **64**, 480.
40 Bruker AXS Topas V5, *General profile and structure analysis software for powder diffraction data, User's manual*, Karlsruhe, Germany, 2014.
41 A. Coelho, *J. Appl. Crystallogr.*, 2018, **51**, 210–218.
42 A. Le Bail, *Powder Diffr.*, 2005, **20**, 316–326.
43 D. B. Williams and C. B. Carter, *Transmission Electron Microscopy – A Textbook for Materials Science*, Springer, Boston, MA, 2009.

2482 | *J. Mater. Chem. A*, 2022, **10**, 2474–2482

This journal is © The Royal Society of Chemistry 2022